

## Supplementary information, figures, and tables

### ”High resolution estimates of Southwest Indian Ridge plate motions, 20 Ma to present”

by *C. DeMets, S. Merkouriev, and D. Sauter*

#### Overview

This supplementary document includes information, figures, and tables that complete the description of Southwest Indian Ridge plate kinematics during the Quaternary and Neogene in the primary manuscript. The supplementary documents also include three text files with all of the magnetic reversal, fracture zone, and transform fault crossings that were used to estimate the rotations that are described in the primary document.

#### List of text file contents

1. *SWIR\_Rvrsl\_Xings.txt*: Crossings of 21 magnetic reversals used in the main document to estimate Nubia-Antarctic, Lwandle-Antarctic, and Somalia-Antarctic finite rotations. Details are given in the file header.
2. *SWIR\_FZ\_Xings.txt*: Crossings of fracture zones used in the main document to estimate Nubia-Antarctic, Lwandle-Antarctic, and Somalia-Antarctic finite rotations. Details are given in the file header.
3. *SWIR\_TF\_Xings.txt*: Crossings of transform faults used in the main document to estimate Nubia-Antarctic, Lwandle-Antarctic, and Somalia-Antarctic finite rotations. Details are given in the file header.

#### S1. Methods

##### *Estimation of finite rotations*

We estimate best-fitting finite rotations via an inversion that simultaneously optimizes the weighted least-squares fits of reconstructed magnetic reversal, fracture zone, and transform fault crossings (Merkouriev & DeMets 2014a). The great-circle fitting criteria used to evaluate the fit of reconstructed magnetic reversal crossings is described by Hellinger (1981) and Chang (1988) and has been employed in many previous plate kinematic studies. The digitized traces of continuous strike-slip faults within transform fault valleys are fit as lines of pure slip (*i.e.* small circles) around the youngest pole of opening (typically the pole for C1n). Fracture zones are assumed to describe the trajectory of a plate through time and are used to constrain the progression of finite rotations that describe a plate’s motion. We adopt the fracture zone fitting criteria described by Shaw & Cande (1990), whereby flow lines that originate at ridge-transform intersections on each side of the ridge are constructed from a time progression of stage rotations that are derived from trial finite rotations. The misfit between the synthetic flow lines and digitized fracture zone flow lines is defined in a least-squares sense via the distance separating the two at each of the observed flow line points.

The fitting function for fracture zone flow lines requires that all of the desired finite rotations for a given plate pair be estimated simultaneously. Consequently, the finite rotations for all 21 magnetic reversals are estimated during a single inversion of all of the magnetic reversal, transform fault, and fracture zone crossings. During the inversion, all 21 finite rotations are corrected identically for the effect of outward displacement. We refer readers to Merkouriev & DeMets (2014a), who describe and validate this method using synthetic data perturbed by Gaussian noise.

#### *Estimation of stage rotations and uncertainties*

We use stage rotations and their covariances, which are derived rigorously from the finite rotations and their covariances, to describe motion during 1-3 Myr intervals. We selected 1-3 Myr-long intervals in order to keep the  $2\text{-}\sigma$  (95%) stage rate uncertainties below  $\pm 1 \text{ mm yr}^{-1}$  given the combined uncertainties in the stage rotations and magnetic reversal age dates. For magnetic reversals whose ages are astronomically calibrated, errors in their estimated ages are unlikely to exceed  $\pm 5000\text{-}10,000$  yrs (Lourens *et al.* 2004). The implied standard error in a stage spreading rate that averages motion over 1.5 Myr, the approximate length of the shortest averaging interval that we use, is only 0.6% of the stage rate or about  $\pm 0.1 \text{ mm yr}^{-1}$  for the slow spreading rates that are typical of the Southwest Indian Ridge. Such errors are a factor of 2-10 smaller than the uncertainties propagated from the rotation covariances and thus do not represent an important limiting factor in our analysis. Although uncertainties in our estimates of outward displacement also affect each of our finite rotations, they do not significantly affect the stage rotations because any bias in the finite rotations due to incorrectly estimated outward displacement is common to all of the finite rotations and is thus canceled upon differencing those rotations to estimate stage rotations.

#### *Data dispersion*

Following Royer & Chang (1991), we use  $\hat{\kappa} = (N - m) / \chi^2$  as a measure of the dispersion of the observations with respect to the predictions of our best-fitting rotations, with  $N$  defined as the number of observations,  $m$  the number of parameters used to fit the data, and  $\chi^2$  the weighted least-squares misfit to the data. Values of  $\hat{\kappa} \simeq 1$  indicate that the data uncertainties are approximately correct, whereas values of  $\hat{\kappa}$  that are significantly greater or less than 1 indicate that the uncertainties are respectively overestimated or underestimated. Rescaling of the data uncertainties by a factor of  $\sqrt{\hat{\kappa}}$  can be used so that the data and hence model uncertainties better approximate the underlying data dispersion.

Given that  $N$  is large ( $> 350$ ) for all three of our data types,  $\hat{\kappa}$  for each type of data is well approximated as follows: (1)  $(N_{mag} - 2P) / \chi^2_P$  for  $N_{mag}$  magnetic reversal crossings grouped into  $P$  paleo-spreading segments, (2)  $N_{fz} / \chi^2_Q$  for  $N_{fz}$  crossings of  $Q$  fracture zones, and (3)  $(N_{tf} - R) / \chi^2_R$  for  $N_{tf}$  crossings of  $R$  transform faults. The total number of parameters  $m$  that are adjusted to fit the data is  $2P+R+3T$ , where  $T$  is the number of rotations (21) that are estimated during the inversion.

#### *Estimation of finite rotation uncertainties*

Uncertainties in finite rotations depend on the geometry of a plate boundary and the number and uncertainties of the data used to find the rotation (Kirkwood *et al.* 1999), provided that the data uncertainties are normally distributed, that magnetic reversal crossings are correctly assigned to conjugate segments that are reconstructed, and that data uncertainties are independent. From reconstructions of high-quality, closely spaced magnetic reversal crossings from the Carlsberg Ridge, Merkouriev & DeMets (2006) demonstrate that the latter assumption is incorrect. They instead find that reconstructions of reversal crossings from numerous spreading segments give rise

to systematic gaps or overlap between segments that are rotated onto their counterparts across the ridge and that the magnitude of these systematic misfits is larger than expected given the well-described random errors in the data. Merkuriev & DeMets (2006) demonstrate that rotation uncertainties determined via data bootstrapping are roughly twice as large as the formal uncertainties.

Here, we estimate rotation uncertainties using the segment-based bootstrapping method described by Merkuriev & DeMets (2006), with one modification. For five of the 61 rotations given in Tables 2, 3, and 4 of the main document, the formal rotation covariances determined using methods described by Chang (1988) and Kirkwood *et al.* (1999) are larger than the bootstrap rotation covariances, based on a comparison of the volumes of the 3-D ellipsoids determined from each set of covariances. In all five cases, the available reversal and fracture zone crossings impose only weak geometric constraints on their best-fitting rotation, thereby giving rise to large formal uncertainties. The bootstrapping method is less sensitive to the plate boundary geometry and thus underestimates the uncertainties in these circumstances. For these five rotations, the formal covariances are adopted as the best estimate of the rotation uncertainties.

The segment-based bootstrap method used for our analysis works as follows: For a given plate boundary, we created 1000 randomized data samples selected from the  $P$  paleo-spreading segments,  $Q$  fracture zone flow lines, and  $T$  transform faults available for that boundary. For each magnetic reversal, we randomly selected  $P$  segments from all of the available segments and added those to the data sample, such that  $21 * P$  randomly selected spreading segments are included in each data sample. Similarly,  $Q$  fracture zones and  $T$  transform faults were also selected randomly from those available and added to the data sample. Each randomized data sample thus includes the same number of spreading segments, fracture zones, and transform faults as the original data sample. The randomized samples however capture a wider range of possible segment combinations and relative segment weights than is the case for the original population of data.

Due to its random nature, the bootstrap procedure may omit particular spreading segments, fracture zones, or transform faults from some data samples, or include them multiple times in others. The effects of any segment-specific errors caused by systematic misidentifications of a particular magnetic anomaly, an imprecisely interpreted fracture zone flow line or transform fault strand, or a variety of other systematic errors that can influence the location of a particular magnetic reversal for a spreading segment are thus well explored via bootstrap data sampling. Uncertainties estimated via this procedure constitute more conservative and estimates of the likely uncertainties in the rotation parameters than the formal rotation covariances, which presume that the underlying data errors are random.

Inversions of each of the 1000 sample data sets to determine their best-fitting sequence of finite rotations yielded 1000 bootstrapped rotations for each reversal included in the inversion. For each reversal, we determined a mean rotation from its 1000 rotation estimates, constituting our preferred rotation estimates (Tables 2-4 of the main document), and a 3x3 orientation matrix and hence the rotation covariances from the 1000 rotation estimates. Following Gramkow (2001), we convert each bootstrap rotation to its equivalent quaternion and then find the renormalized mean of each component of the quaternion. This method approximates the true mean within 1% for rotations with angles smaller than 40 degrees (Gramkow 2001).

## **S2. Dispersion and weighting of magnetic reversal crossings**

Before estimating best-fitting rotations for the Lwandle-Antarctic, Nubia-Antarctic, and Somalia-Antarctic plate pairs, we inverted all crossings of reversals C1n through C6no for each plate pair to determine realistic location uncertainties for the reversal crossings. Fig. S1 shows the dispersions

of the individual reversal crossing misfits for each of the 21 reversals and each of the three plate pairs. The dispersions are consistently between 1 km and 2 km for all of the reversals and all three plate pairs, the same as dispersions we find along other slow-spreading boundaries (Merkouriev & DeMets 2014ab). Based on the observed dispersion values, we assigned one-sigma uncertainties of  $\pm 1.4$  km to all of the reversal crossings for C1n to C3An.2 and  $\pm 1.6$  km uncertainties to reversal crossings older than C3An.2. The assigned uncertainties assure correct relative weighting of reversal crossings of different ages within our inversions for best-fitting rotations and are also necessary to weight the reversal crossings correctly with respect to the transform fault and fracture zone crossings. The data uncertainties are not however propagated into the rotation covariances, which are instead estimated via data bootstrapping.

### S3. Reconstructions

Figures S2 to S5 variously depict Nubia-Antarctic flow lines (Fig. S2) for three fracture zones at the western end of the Southwest Indian Ridge and several areas of dense magnetic survey coverage along the Lwandle-Antarctic (Fig. S3) and Somalia-Antarctic (Figs. S4 and S5) plate boundaries. The maps in Figs. S3-S5 are located in Figure 2 of the main document. Brief discussions of these reconstructions are given in Section 4.3 of the main document.

### S4. Misfit statistics

Figure S6 summarizes the misfits of the best-fitting rotations from Tables 1-3 for the Nubia-Antarctic, Lwandle-Antarctic, and Somalia-Antarctic plate pairs. The weighted misfits for the 4822 individual reversal crossings are normally distributed (Fig. S6-A), indicating that the reversal crossings are dispersed randomly about their best reconstructed great-circle segments. Overall,  $\hat{\kappa} = 1.00$  for the 4822 magnetic reversal crossings, equal to the value of 1.0 expected for data whose uncertainties are correctly determined. The wrms misfits for the 21 magnetic reversals range from 1.3 to 2.5 km (Table 1), with nearly all of the individual misfits smaller than 4 km (Fig. S6-B) and comparable levels of misfit everywhere along the ridge.

Fig. S6-C characterizes the systematic component of the misfits for all 556 reconstructed spreading segments, with under-rotations corresponding to a gap between the stationary and rotated reversal crossings that define a reconstructed spreading segment and over-rotations corresponding to overlap of the stationary and reconstructed reversal crossings. Two-thirds (68.3%) of the segment misfits are 2.1 km or smaller (red lines in Fig. S6-C), consistent with results reported for the Carlsberg Ridge and Eurasia-North America plate boundary (Merkouriev & DeMets 2006, 2008). For comparison, a Monte Carlo analysis of synthetic reversal crossings that reproduce both the geometry and distribution of our data indicates that 68.3% of the over-rotations or under-rotations for the reconstructed synthetic data should be only 1.0 km or smaller when the synthetic reversal locations are perturbed by random  $1-\sigma$  location uncertainties equal to those of our observations (*e.g.*  $\pm 1.5$  km). The observed segment misfits are thus a factor-of-two larger than expected given the underlying random errors.

As is described in our previous work (*i.e.* Merkouriev & DeMets 2006, 2008), we interpret these larger-than-expected spreading segment misfits as evidence that a variety of processes may shift the location of a magnetic reversal for some or all of an individual spreading segment toward or away from its idealized location. Such processes may include variations in the magnitude of outward displacement for different spreading segments due to differences in their accretionary or thermal histories, and effects of seafloor topography and anomalous skewness on the shapes

of magnetic anomalies. The bootstrap method described in Supplementary Section S1 generates rotation uncertainty estimates that account for these likely systematic errors.

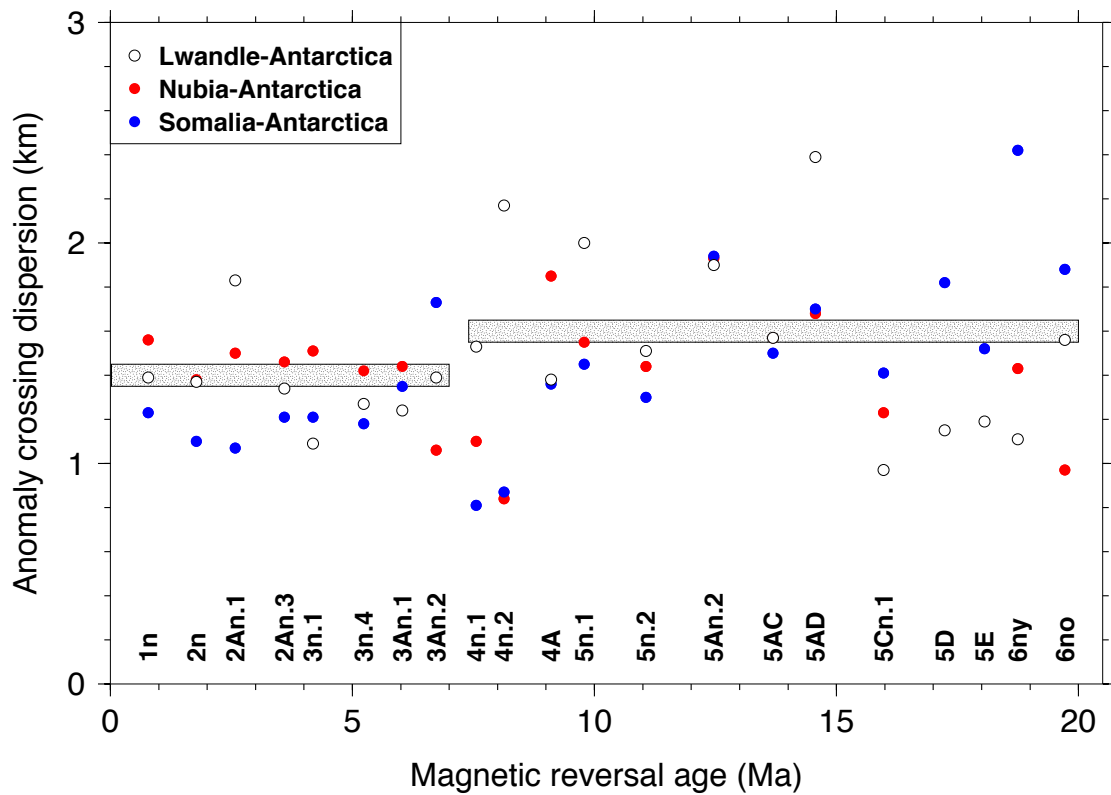


Fig. S1. Dispersions of magnetic reversal crossing misfits for the Lwandle-Antarctica, Nubia-Antarctica, and Somalia-Antarctica plate pairs for C1n through C6no, where the misfit to an individual reversal crossings is defined as the great-circle distance between the reversal crossing and its best-fitting, reconstructed great circle segment. The dispersion is defined here as the standard deviation of data misfits adjusted for the number of parameters that were adjusted to fit the data. The two shaded bars show the standard errors that we assigned to the individual reversal crossings based on the dispersions for reversals 1n through 3An.2 and 4n.1 through 6no. The larger scatter in the dispersions for the older reversals is caused by sparser shipboard coverage of the older reversals, which complicates their identification and makes it more difficult to match paleo-spreading segments across the spreading center.

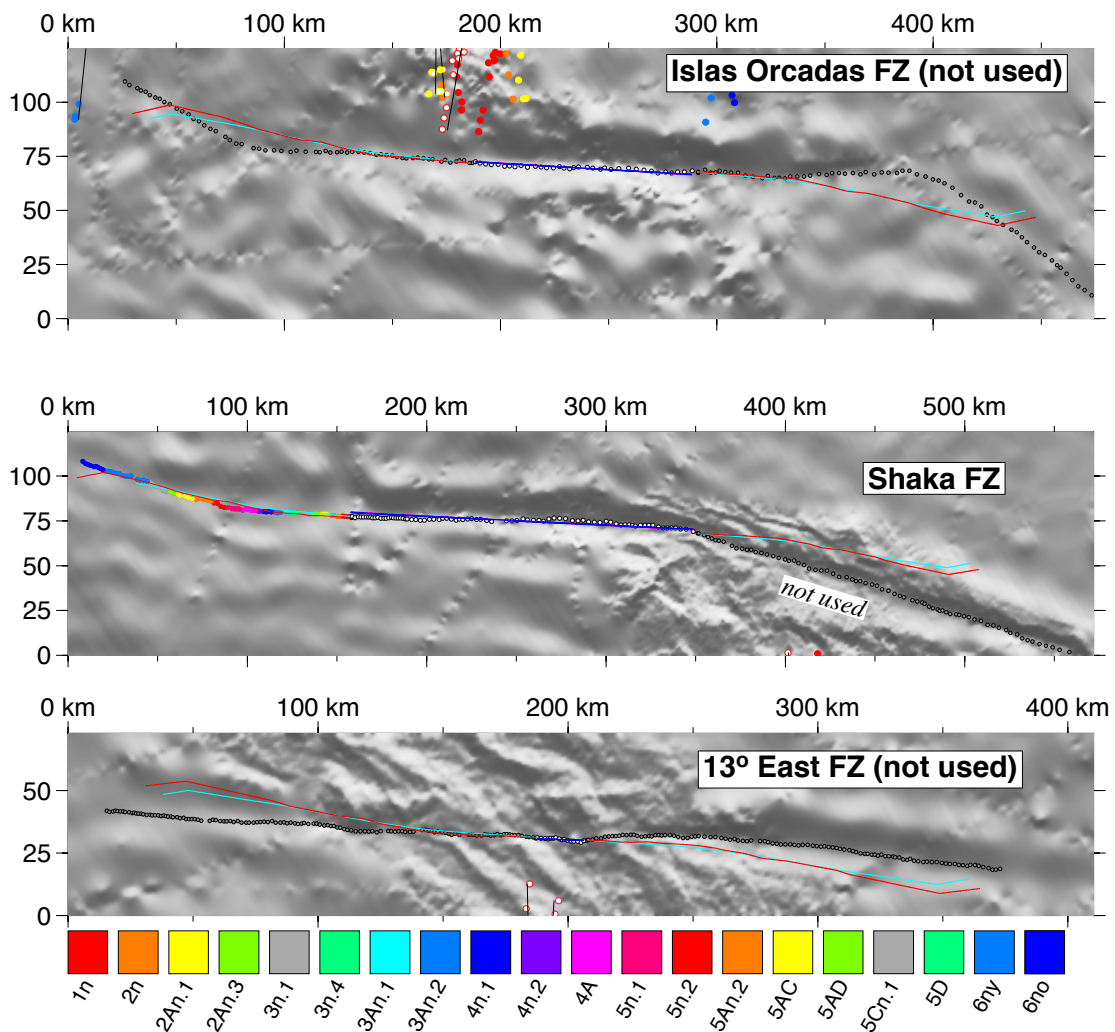


Fig. S2. Digitized traces of the Islas Orcadas, Shaka, and 13°E fracture zones and the flow lines predicted for these features by Nubia-Antarctica stage rotations determined from the best-fitting and noise-reduced finite rotations in Tables 2, S1, and S4. Red and aquamarine flow lines are predicted from the best-fitting and noise-reduced rotations, respectively. Only the southern half of the Shaka fracture zone (depicted on the left side of the panel) was used to estimate the Nubia-Antarctica rotations. The traces of the Islas Orcadas, 13°E, and northern half of the Shaka fracture zones are inconsistent with the well-defined traces of the other Nubia-Antarctica fracture zones and are excluded from the rotation estimation. The transform faults for all three features were however used to estimate the rotations; small-circle fits for the youngest (C1n) opening pole to the transform fault segments of each flow line are indicated by the blue lines. Circles are color-coded by age according to the legend below the figure. Maps are oblique Mercator projections about the Nubia-Antarctica opening pole for C5n.2 (Table 2).

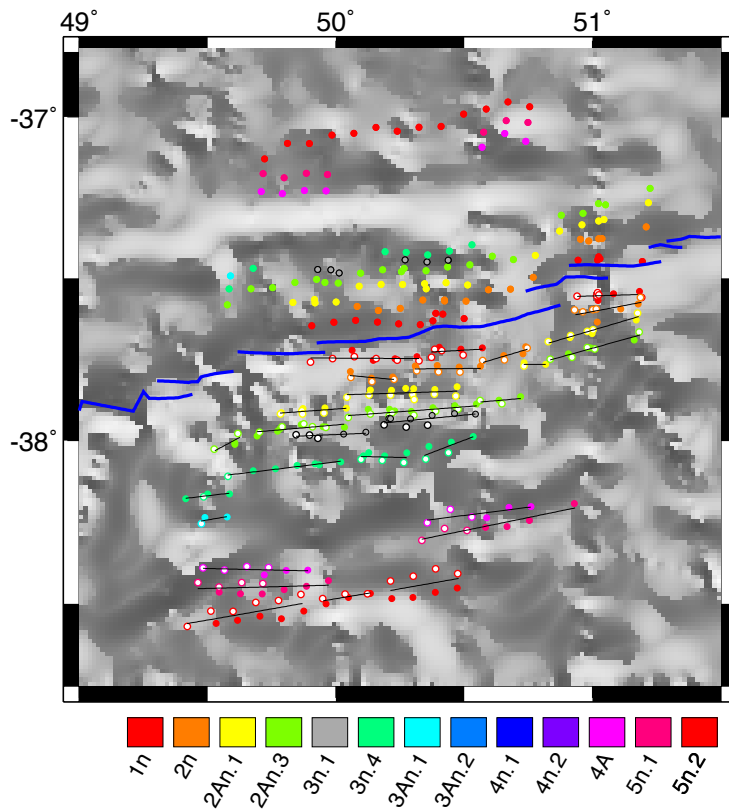


Fig. S3. Reconstructions of Lwandle-Antarctic plate magnetic lineations from rotations in Table 3 and corrected for 2 km of outward displacement. Solid circles show stationary magnetic reversal crossings identified from shipboard and airborne data (also shown in Fig. 2A). Open circles show Lwandle plate reversal crossings rotated onto the Antarctic plate. Black lines show great circle segments that best fit the stationary and rotated reversal crossings that define paleospreading segments. Blue line shows present plate boundary. See Fig. 2A for map location.

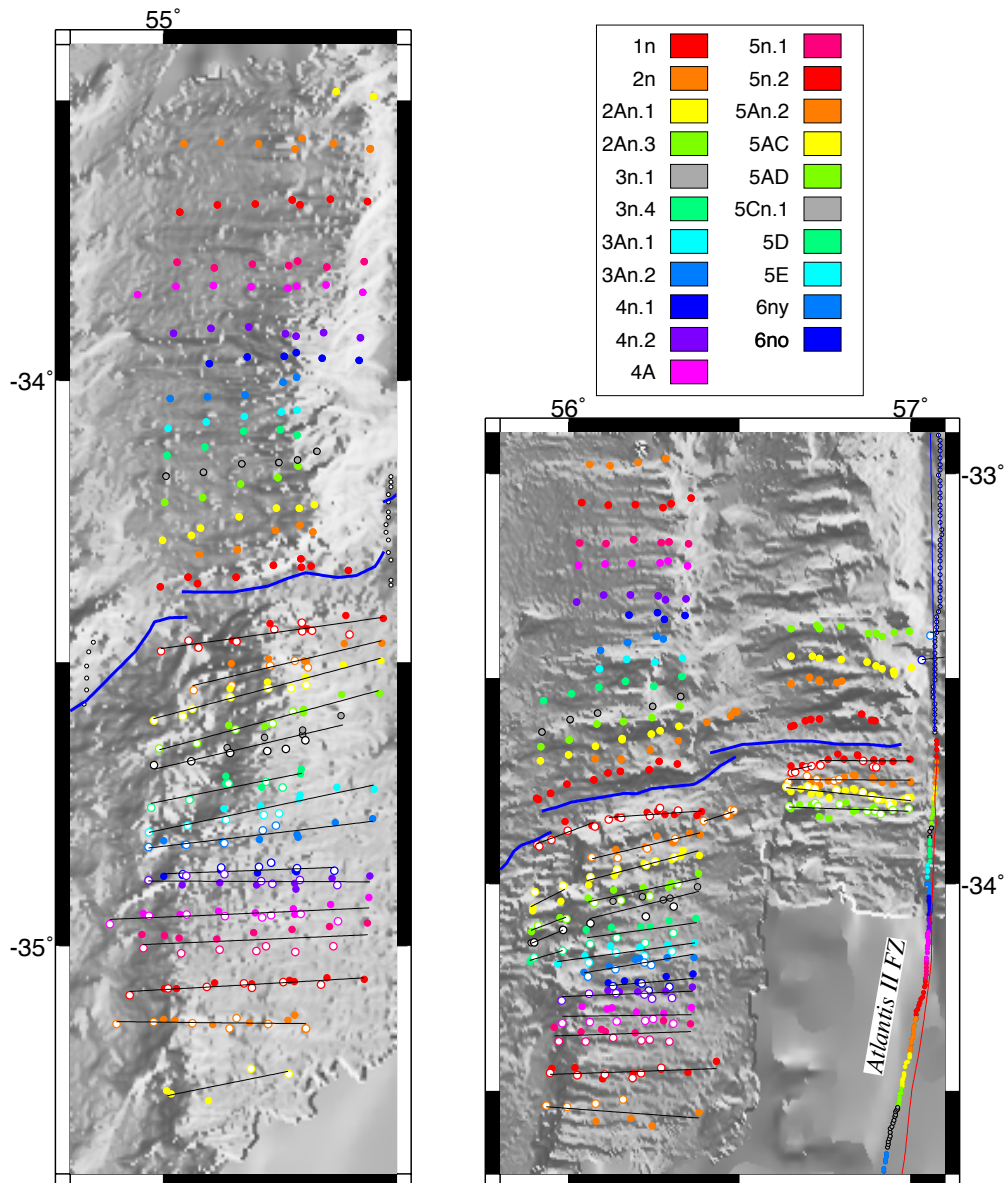


Fig. S4. Reconstructions of Somalia-Antarctic plate magnetic lineations from rotations in Table 4 and corrected for 2 km of outward displacement. Solid circles show unrotated magnetic reversal crossings identified from shipboard and airborne data (also shown in Fig. 2A). Open circles show Somalia plate reversal crossings rotated onto the Antarctic plate. Black lines show great circle segments that best fit the ensemble of stationary and rotated reversal crossings. Blue line shows present plate boundary. See Fig. 2A for map locations. Abbreviation: "NTD", non-transform discontinuity.

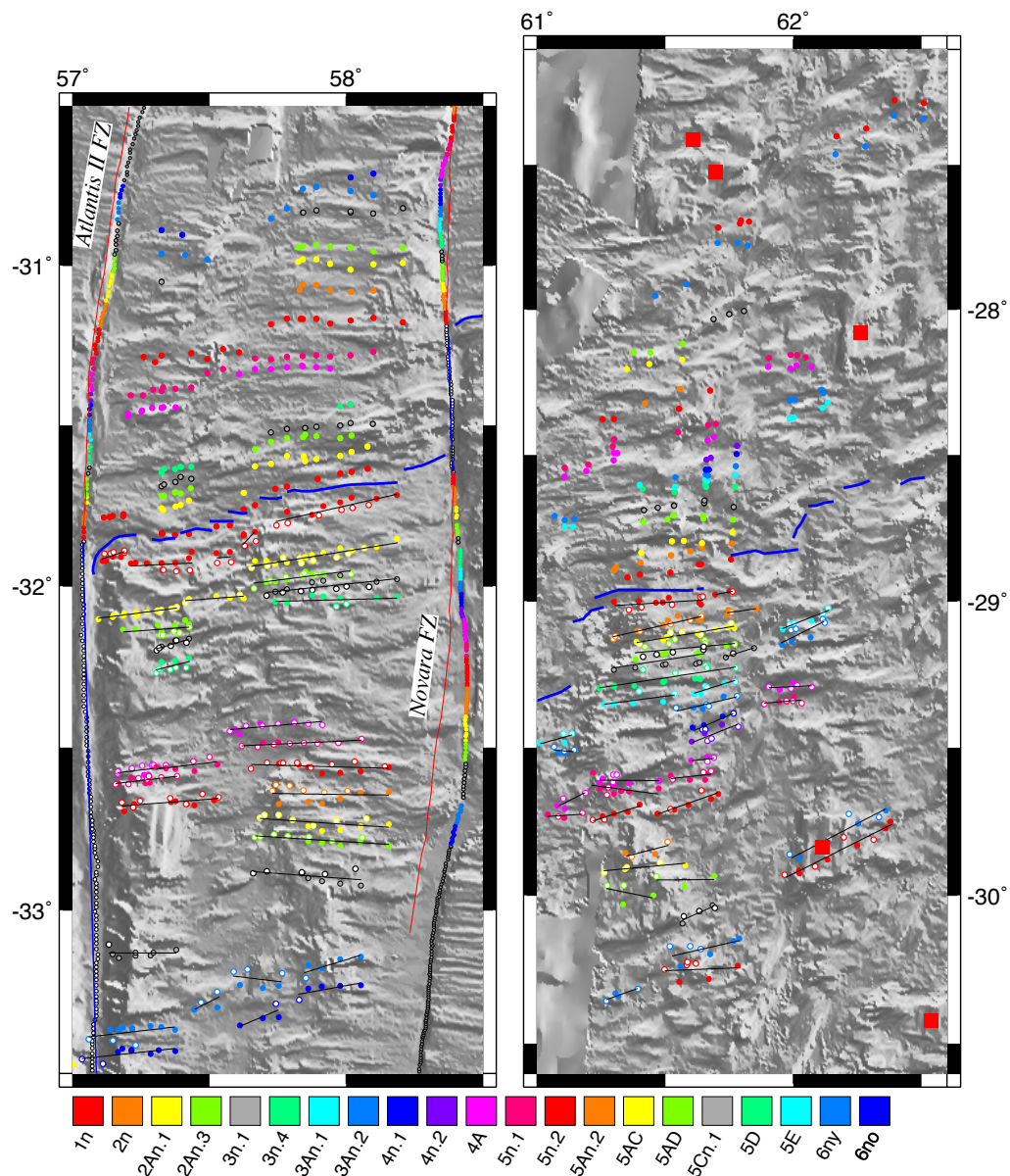


Fig. S5. Reconstructions of Somalia-Antarctic plate magnetic lineations from rotations in Table 4 and corrected for 2 km of outward displacement. Solid circles show unrotated magnetic reversal crossings identified from shipboard and airborne data (also shown in Fig. 2A). Open circles show Somalia plate reversal crossings rotated onto the Antarctic plate. Black lines show great circle segments that best fit the ensemble of stationary and rotated reversal crossings. Blue line shows present plate boundary. See Fig. 2A for map locations. Red squares show locations of corrugated surfaces on the footwalls of axial detachment faults identified by Cannat *et al.* [2009].

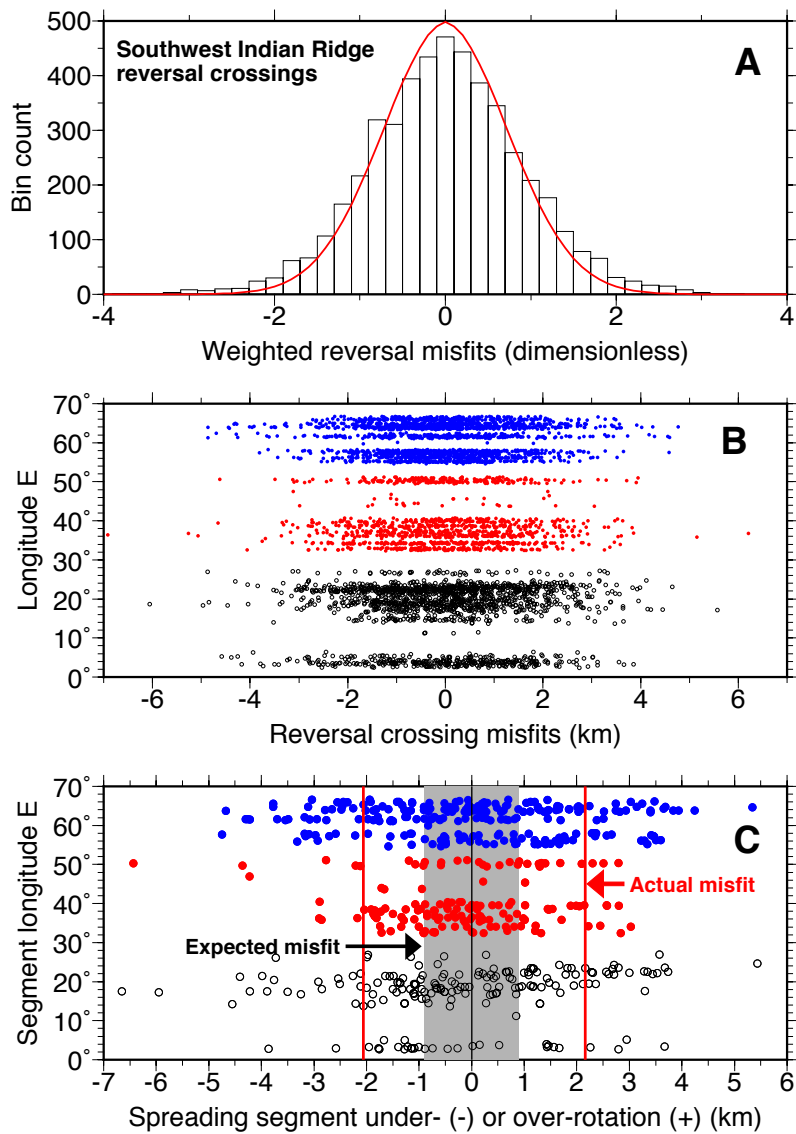


Fig. S6. A - Histogram of misfits for 4822 reconstructed crossings of reversals C1n to 6no, normalized by their assigned uncertainties. Red curve shows the distribution of weighted residuals expected for an equivalent number of degrees of freedom (4822 minus 1234, the number of fitting parameters) for data with normally distributed errors and correctly estimated uncertainties. B - Residual distances of reversal crossings from their reconstructed great circle segment versus location, Southwest Indian Ridge. Black, red, and blue circles respectively show residual distances for Nubia-Antarctica, Lwandle-Antarctica, and Somalia-Antarctica reversal crossings. C - Systematic over- and under-rotations of reversal crossings averaged by segment for each of the 556 rotated anomaly segments for C1n to C6no. Color coding follows (B). The red lines encompass 68.3% of the observed segment misfits after adjusting for the number of fitting parameters. Shaded area spans the expected one-sigma limit for segment over- and under-rotations based on a Monte Carlo simulation of the Southwest Indian Ridge reversal crossings with realistic one-sigma uncertainties of  $\pm 1.5$  km (Fig. S1). That the observed misfits are larger than those expected for synthetic data perturbed solely by random errors indicates that both random and systematic errors contribute to reversal location uncertainties (see text).

## References

- Cannat, M., Sauter, D., Escartin, J., Lavier, L., & Picazo, S., 2009. Oceanic corrugated surfaces and the strength of the axial lithosphere at slow spreading ridges, *Earth Planet. Sci. Lett.*, **288**, 174–183, doi: 10.1016/j.epsl.2009.09.020.
- Chang, T., 1988. Estimating the relative rotation of two tectonic plates from boundary crossings, *J. Am. Statistical Assoc.*, **83**, 1178–1183.
- Gramkow, C., 2001. On averaging rotations, *J. Mathematical Imaging and Vision*, **15**, 7–16.
- Hellinger, S. J., 1981. The uncertainties of finite rotations in plate tectonics, *J. Geophys. Res.*, **86**, 9312–9318.
- Iaffaldano, G., Hawkins, R., Bodin, T., & Sambridge, M., 2014. REDBACK: Open-source software for efficient noise-reduction in plate kinematic reconstructions, *Geochem. Geophys. Geosys.*, **15**, 1663–1670.
- Kirkwood, B. H., Royer, J.-Y., Chang, T. C., & Gordon, R. G., 1999. Statistical tools for estimating and combining finite rotations and their uncertainties, *Geophys. J. Int.*, **137**, 408–428.
- Lourens, L., Hilgen, F. J., Laskar, J., Shackleton, N. J., & Wilson, D., 2004. The Neogene Period, *A Geologic Time Scale 2004*, 409–440 Gradstein, F., J. Ogg, & A. Smith, Cambridge University Press, London.
- Merkouriev, S., & DeMets, C., 2006. Constraints on Indian plate motion since 20 Ma from dense Russian magnetic data: Implications for Indian plate dynamics, *Geochem. Geophys. Geosyst.*, **7**, Q02002, doi:10.1029/2005GC001079.
- Merkouriev, S., & DeMets, C., 2008. A high-resolution model for Eurasia-North America plate kinematics since 20 Ma, *Geophys. J. Int.*, **173**, 1064–1083, doi:10.1111/j.1365-246X.2008.03761.x.
- Merkouriev, S., & DeMets, C., 2014a. High-resolution estimates of Nubia-North America plate motion: 20 Ma to present, *Geophys. J. Int.*, **196**, 1299–1310, doi: 10.1093/gji/ggt463.
- Merkouriev, S. & DeMets, C., 2014b. High-resolution Quaternary and Neogene reconstructions of Eurasia-North America plate motion, *Geophys. J. Int.*, doi: 10.1093/gji/ggu142.
- Royer, J.-Y. & Chang, T., 1991. Evidence for relative motions between the Indian and Australian plates during the last 20 Myr from plate tectonic reconstructions: Implications for the deformation of the Indo-Australian plate, *J. Geophys. Res.*, **96**, 11779–11802.
- Shaw, P. R., & Cande, S. C., 1990. High-resolution inversion for South Atlantic plate kinematics using joint altimeter and magnetic anomaly data, *J. Geophys. Res.*, **95**, 2625–2644.

Table S1. Nubia-Antarctic finite rotations after noise reduction

Chron	Lat.	Long.	$\Omega$	Covariances					
				a	b	c	d	e	f
	(°N)	(°E)	(degrees)						
1n	-6.58	328.48	-0.115	49.8	-30.4	-35.6	18.7	21.9	25.8
2n	-7.29	328.69	-0.259	60.2	-36.3	-42.5	22.2	26.1	30.6
2An.1	-7.90	328.90	-0.375	70.9	-42.3	-49.4	25.7	30.2	35.4
2An.3	-8.31	329.07	-0.522	89.1	-52.7	-61.3	31.9	37.3	43.7
3n.1	-8.27	329.07	-0.607	103.5	-61.0	-70.9	37.0	43.4	50.9
3n.4	-7.75	328.87	-0.750	117.3	-69.9	-81.5	42.6	49.9	58.6
3An.1	-7.15	328.67	-0.851	159.5	-96.3	-112.5	58.9	69.1	81.1
3An.2	-6.72	328.63	-0.944	211.5	-128.0	-149.7	78.4	92.0	108.0
4n.1	-6.42	328.75	-1.060	221.3	-133.2	-155.5	81.3	95.4	111.9
4n.2	-6.24	328.88	-1.148	219.4	-131.0	-152.7	79.8	93.5	109.7
4A	-5.96	329.14	-1.303	211.4	-124.4	-144.4	75.3	88.1	103.2
5n.1	-5.71	329.30	-1.411	210.5	-122.5	-141.9	74.0	86.5	101.4
5n.2	-5.40	329.64	-1.611	199.6	-114.0	-131.3	68.3	79.7	93.3
5An.2	-5.38	330.12	-1.838	186.5	-103.4	-118.2	61.5	71.6	83.7
5AC	-5.55	330.56	-2.048	156.9	-83.2	-93.9	50.0	58.3	68.6
5AD	-5.68	330.83	-2.192	169.0	-86.6	-96.9	52.8	61.8	73.2
5Cn.1	-5.84	331.11	-2.422	305.6	-154.6	-172.5	93.6	109.4	129.3
6ny	-4.05	330.44	-2.854	388.8	-184.3	-201.7	124.1	148.5	180.9
6no	-1.70	327.38	-2.981	304.3	-164.6	-186.2	118.2	144.5	179.5

These rotations were determined from the best-fitting Nubia-Antarctica finite rotations and covariances in Table 2 using Bayesian noise reduction as implemented in REDBACK software (Iaffaldano *et al.* 2014). The rotations reconstruct movement of the Nubia plate relative to the Antarctic plate and include corrections for 5 km of outward displacement described in the text. The rotation angles  $\Omega$  are positive anti-clockwise. The Cartesian rotation covariances are calculated in a Nubia-fixed reference frame and have units of  $10^{-9}$  radians<sup>2</sup>.

Table S2. Lwandle-Antarctic finite rotations after noise reduction

Chron	Lat.	Long.	$\Omega$	Covariances*					
				a	b	c	d	e	f
1n	6.57	318.19	-0.097	9.8	-8.6	-11.6	7.7	10.4	14.0
2n	6.85	318.60	-0.220	16.1	-13.9	-18.5	12.3	16.4	22.1
2An.1	7.05	318.95	-0.319	24.5	-21.0	-27.6	18.3	24.3	32.4
2An.3	7.26	319.40	-0.445	39.5	-33.3	-43.7	28.6	37.8	50.0
3n.1	7.37	319.64	-0.518	50.4	-42.1	-55.0	35.9	47.3	62.4
3n.4	7.56	319.99	-0.649	69.1	-57.1	-74.2	48.1	62.9	82.6
3An.1	7.72	320.20	-0.753	76.6	-62.6	-81.0	52.4	68.4	89.6
3An.2	7.87	320.35	-0.847	80.3	-65.0	-83.7	54.2	70.6	92.4
4n.1	8.05	320.49	-0.956	82.5	-66.0	-84.6	54.8	71.3	93.4
4n.2	8.17	320.60	-1.036	80.1	-63.3	-80.6	52.5	68.2	89.5
4A	8.38	320.77	-1.176	69.3	-53.3	-67.1	44.2	57.4	75.6
5n.1	8.53	320.88	-1.272	63.1	-47.1	-58.5	39.1	50.9	67.5
5n.2	8.71	321.15	-1.451	57.8	-41.2	-50.2	34.3	44.6	59.5
5An.2	8.87	321.45	-1.653	63.0	-43.4	-52.0	36.0	46.8	62.6
5AC	9.07	321.66	-1.836	80.9	-55.6	-66.5	45.8	59.4	79.4
5AD	9.25	321.77	-1.955	85.5	-57.6	-68.4	47.6	61.7	82.7
5Cn.1	9.57	321.89	-2.127	102.7	-70.1	-83.8	57.2	74.0	98.3
5D	9.93	321.92	-2.308	74.8	-45.0	-50.1	38.3	50.2	69.5
5E	10.18	321.88	-2.424	65.5	-33.2	-32.7	30.0	40.1	58.6
6ny	10.41	321.80	-2.516	73.5	-31.5	-26.2	30.2	41.3	63.4
6no	10.76	321.60	-2.638	163.4	-75.2	-65.4	69.1	93.5	143.2

These rotations were determined from the best-fitting Lwandle-Antarctica finite rotations and covariances in Table 3 using Bayesian noise reduction as implemented in REDBACK software (Iafaldano *et al.* 2014). The finite rotations reconstruct movement of the Lwandle plate relative to the Antarctic plate and include corrections for 2 km of outward displacement described in the text. The rotation angles  $\Omega$  are positive anti-clockwise. The Cartesian rotation covariances are calculated in a Lwandle-fixed reference frame and have units of  $10^{-9}$  radians<sup>2</sup>.

Table S3. Somalia-Antarctic finite rotations after noise reduction

Chron	Lat.	Long.	$\Omega$	Covariances*					
				a	b	c	d	e	f
1n	5.59	319.22	-0.094	6.9	-5.9	-7.7	5.1	6.7	8.9
2n	6.04	319.30	-0.213	10.7	-9.1	-12.0	7.9	10.4	13.7
2An.1	6.30	319.36	-0.308	14.5	-12.3	-16.2	10.6	14.0	18.5
2An.3	6.35	319.53	-0.428	20.9	-17.6	-23.1	15.1	19.8	26.2
3n.1	6.32	319.71	-0.497	26.2	-21.9	-28.7	18.6	24.5	32.2
3n.4	6.20	320.04	-0.619	38.1	-31.6	-41.2	26.5	34.7	45.5
3An.1	6.20	320.17	-0.714	45.0	-37.2	-48.3	31.1	40.6	53.0
3An.2	6.30	320.18	-0.800	48.0	-39.5	-51.3	33.0	43.1	56.4
4n.1	6.48	320.14	-0.902	49.2	-40.3	-52.2	33.8	44.1	57.8
4n.2	6.57	320.15	-0.979	49.2	-39.9	-51.5	33.5	43.8	57.6
4A	6.96	319.99	-1.116	38.9	-31.0	-39.6	26.3	34.5	45.8
5n.1	7.36	319.85	-1.211	35.6	-27.3	-34.2	23.4	30.9	41.6
5n.2	7.28	320.61	-1.382	31.3	-23.4	-29.0	19.6	25.7	34.2
5An.2	7.05	321.53	-1.567	38.8	-27.6	-33.6	22.6	29.3	38.7
5AC	7.33	321.76	-1.736	47.6	-33.3	-40.3	27.1	35.0	46.3
5AD	7.64	321.75	-1.855	50.6	-34.6	-41.4	28.4	36.7	48.9
5Cn.1	8.26	321.58	-2.049	43.7	-28.3	-32.8	23.7	30.9	42.0
5D	9.02	321.08	-2.228	44.0	-29.1	-34.1	24.8	32.6	44.5
5E	9.59	320.56	-2.355	31.5	-19.7	-22.2	17.4	23.1	32.5
6ny	10.06	320.07	-2.461	29.0	-17.2	-18.6	15.6	21.1	30.4
6no	10.72	319.35	-2.611	33.9	-15.4	-12.7	15.2	21.2	33.7

These rotations were determined from the best-fitting Somalia-Antarctica finite rotations and covariances in Table 4 using Bayesian noise reduction as implemented in REDBACK software (Iafaldano *et al.* 2014). The finite rotations reconstruct movement of the Somalia plate relative to the Antarctic plate and include corrections for 2 km of outward displacement described in the text. The rotation angles  $\Omega$  are positive anti-clockwise. The Cartesian rotation covariances are calculated in a Somalia-fixed reference frame and have units of  $10^{-9}$  radians<sup>2</sup>.

Table S4. Nubia-Antarctic stage angular velocities from REDBACK

Age(y)	Age(o)	Lat.	Long.	$\dot{\omega}$	Covariances					
(Ma)	(Ma)	(°N)	(°E)	(degrees)	a	b	c	d	e	f
0.000	0.781	-6.37	328.56	0.144	6.53	-3.68	-0.63	2.78	0.42	1.92
0.781	1.778	-7.68	328.94	0.144	2.54	-1.10	-0.08	1.41	-0.02	3.12
1.778	2.581	-9.42	329.62	0.144	2.26	-0.40	0.14	1.95	-0.54	6.48
2.581	3.596	-9.80	329.77	0.144	2.17	-0.12	0.28	2.26	-0.83	7.57
3.596	4.187	-8.14	329.18	0.143	3.43	0.43	0.95	4.26	-1.40	15.15
4.187	5.235	-5.70	327.82	0.143	4.87	-0.39	0.48	4.82	-1.37	14.31
5.235	6.033	-2.57	326.71	0.141	8.11	-0.26	0.35	8.86	-3.99	28.64
6.033	6.733	-1.96	327.73	0.142	7.92	0.21	1.14	8.71	-3.84	37.27
6.733	7.528	-4.02	329.83	0.145	5.72	1.30	1.92	7.27	-2.48	34.72
7.528	8.108	-4.36	330.81	0.148	7.64	2.68	3.45	10.76	-3.18	52.02
8.108	9.105	-4.54	331.76	0.151	6.61	2.15	2.22	9.52	-3.57	41.19
9.105	9.786	-1.64	330.96	0.154	8.58	4.59	4.37	14.43	-5.90	72.25
9.786	11.056	-1.74	331.24	0.157	5.43	2.54	1.53	8.78	-4.06	41.43
11.056	12.474	-5.73	333.75	0.160	4.84	1.85	1.21	7.11	-2.66	32.51
12.474	13.739	-8.46	335.37	0.161	5.20	2.52	0.84	8.78	-4.98	40.25
13.739	14.609	-8.92	335.17	0.161	6.62	4.09	3.34	12.57	-6.87	65.73
14.609	15.974	-8.43	333.30	0.160	8.76	5.29	5.56	15.74	-7.66	83.34
15.974	18.748	5.69	325.95	0.162	9.63	7.79	-0.70	21.85	-16.91	87.39
18.748	19.722	52.32	284.90	0.375	160.06	171.16	-84.29	384.81	-273.83	1078.50

These angular velocities specify Nubia plate motion relative to the Antarctic plate during the time period given in the first two columns, as determined from the REDBACK noise-reduction software (Iaffaldano *et al.* 2014). They include corrections for 5 km of outward displacement, as described in the text. The angular rotation rates  $\dot{\omega}$  are positive anti-clockwise. The Cartesian angular velocity covariances are calculated in a Nubia-fixed reference frame and have units of  $10^{-8}$  radians<sup>2</sup> Myr<sup>-2</sup>.

Table S5. Lwandle-Antarctic stage angular velocities from REDBACK

Age(y)	Age(o)	Lat.	Long.	$\dot{\omega}$	Covariances					
(Ma)	(Ma)	(°N)	(°E)	(degrees)	a	b	c	d	e	f
0.000	0.781	6.57	318.20	0.124	1.54	-0.77	0.17	1.37	-0.18	0.11
0.781	1.778	7.07	318.92	0.124	0.98	-0.31	0.07	0.87	-0.11	0.19
1.778	2.581	7.49	319.72	0.124	1.01	-0.21	0.07	0.92	-0.08	0.31
2.581	3.596	7.80	320.55	0.123	1.12	-0.14	0.09	1.05	-0.06	0.36
3.596	4.187	8.06	321.06	0.124	1.60	-0.08	0.04	1.50	-0.15	0.57
4.187	5.235	8.29	321.41	0.125	1.66	-0.35	0.08	1.50	-0.18	0.57
5.235	6.033	8.71	321.49	0.131	2.14	-0.89	0.20	1.82	-0.22	0.65
6.033	6.733	9.14	321.49	0.134	2.19	-0.63	0.02	1.90	-0.31	1.03
6.733	7.528	9.45	321.63	0.136	2.02	-0.16	-0.08	1.84	-0.28	1.15
7.528	8.108	9.61	321.91	0.139	2.17	0.12	-0.08	2.08	-0.19	1.39
8.108	9.105	9.98	322.03	0.140	1.79	0.20	-0.26	1.72	-0.27	1.50
9.105	9.786	10.30	322.14	0.141	3.33	1.15	-0.89	3.21	-0.77	2.82
9.786	11.056	10.02	323.08	0.141	2.19	0.63	-0.55	2.14	-0.46	2.17
11.056	12.474	10.05	323.60	0.142	2.82	0.54	-0.94	2.63	-0.77	3.68
12.474	13.739	10.93	323.56	0.145	4.62	-1.53	0.11	3.80	-0.70	2.75
13.739	14.609	11.96	323.40	0.138	5.15	-1.52	0.30	4.27	-0.66	2.67
14.609	15.974	13.25	323.17	0.126	12.55	-6.96	1.67	9.09	-1.95	3.26
15.974	17.235	14.08	322.21	0.144	9.72	-1.68	0.00	8.28	-1.55	5.29
17.235	18.056	15.29	321.03	0.142	13.18	3.08	-1.82	13.09	-2.57	9.00
18.056	18.748	16.38	319.54	0.133	20.67	13.21	-3.94	23.42	-3.15	14.44
18.748	19.722	17.63	317.21	0.127	60.12	38.81	-7.25	65.27	-3.96	39.52

These angular velocities specify Lwandle plate motion relative to the Antarctic plate during the time period given in the first two columns, as determined from the REDBACK noise-reduction software (Iaffaldano *et al.* 2014). They include corrections for 2 km of outward displacement, as described in the text. The angular rotation rates  $\dot{\omega}$  are positive anti-clockwise. The Cartesian angular velocity covariances are calculated in a Lwandle-fixed reference frame and have units of  $10^{-8}$  radians<sup>2</sup> Myr<sup>-2</sup>.

Table S6. Somalia-Antarctic stage angular velocities from REDBACK

Age(y)	Age(o)	Lat.	Long.	$\dot{\omega}$	Covariances					
(Ma)	(Ma)	(°N)	(°E)	(degrees)	a	b	c	d	e	f
0.000	0.781	5.59	319.22	0.120	1.21	-0.71	0.12	1.01	-0.10	0.19
0.781	1.778	6.40	319.37	0.120	0.75	-0.17	0.03	0.71	-0.02	0.51
1.778	2.581	6.86	319.50	0.119	1.00	0.05	-0.05	1.01	0.00	1.10
2.581	3.596	6.51	319.97	0.118	1.22	0.16	-0.06	1.27	0.01	1.34
3.596	4.187	6.11	320.81	0.117	2.60	0.77	-0.28	2.79	-0.02	3.32
4.187	5.235	5.73	321.39	0.117	2.65	0.66	-0.35	2.80	-0.20	3.04
5.235	6.033	6.23	320.98	0.119	3.36	1.11	-0.32	3.72	-0.04	4.09
6.033	6.733	7.10	320.29	0.123	4.73	1.52	-0.33	5.25	0.00	5.36
6.733	7.528	7.89	319.79	0.128	5.58	2.13	-0.58	6.24	-0.14	6.45
7.528	8.108	7.58	320.28	0.133	7.60	4.13	-1.35	8.79	-0.34	10.70
8.108	9.105	9.72	318.84	0.138	6.98	4.08	-1.76	7.86	-1.13	8.23
9.105	9.786	12.07	318.16	0.140	15.22	10.42	-7.48	16.10	-5.27	21.64
9.786	11.056	6.72	325.99	0.135	6.28	4.89	-2.66	7.00	-1.70	8.34
11.056	12.474	5.39	328.27	0.132	7.25	5.46	-3.98	8.32	-3.15	11.15
12.474	13.739	9.96	323.95	0.133	4.82	3.24	-1.80	5.82	-0.84	9.34
13.739	14.609	12.21	321.44	0.137	7.58	4.83	-2.22	9.17	-0.59	14.20
14.609	15.974	14.09	319.88	0.143	6.97	3.30	-1.72	7.87	-0.81	10.46
15.974	17.235	17.43	314.98	0.144	8.35	3.53	-1.62	9.39	-1.00	10.78
17.235	18.056	19.09	311.04	0.159	11.89	6.87	-2.54	14.01	-1.82	12.22
18.056	18.748	19.74	308.92	0.159	14.99	11.48	-2.99	18.32	-1.72	12.86
18.748	19.722	20.72	306.98	0.160	23.14	18.92	-3.22	27.80	-1.93	13.54

These angular velocities specify Somalia plate motion relative to the Antarctic plate during the time period given in the first two columns, as determined from the REDBACK noise-reduction software (Iaffaldano *et al.* 2014). They include corrections for 2 km of outward displacement, as described in the text. The angular rotation rates  $\dot{\omega}$  are positive anti-clockwise. The Cartesian angular velocity covariances are calculated in a Somalia-fixed reference frame and have units of  $10^{-8}$  radians<sup>2</sup> Myr<sup>-2</sup>.